Application of an Additional Excitation in Inverter-Fed Induction Motors for Air-Gap Eccentricity Diagnosis

Guillermo Bossio, *Student Member, IEEE*, Cristian De Angelo, *Member, IEEE*, Jorge Solsona, *Senior Member, IEEE*, Guillermo O. García, *Senior Member, IEEE*, and María I. Valla, *Senior Member, IEEE*

***Abstract*—In this paper, the application of an additional excitation in induction motor (IM) drives for static, dynamic, and mixed eccentricity diagnosis is proposed. The additional excitation consists in a predefined inverter-switching pattern that is applied on the motor for a short time, while the fundamental excitation is canceled. This excitation was used previously to implement a position estimation strategy. The strategy obtains information about the rotor position from the motor saliencies effects over the zero-sequence voltage. The air-gap eccentricity is a kind of saliency that affects the zero-sequence voltage and allows the use of the additional excitation for eccentricity diagnosis. For the evaluation of the feasibility of this proposal, a multiple-coupled circuit model of the IM is used. The effects of series and series–parallel stator winding connections on the diagnosis signals are shown. Experimental results to validate the proposal are also given. These results show that it is possible to use the diagnosis strategy in a self-commissioning scheme.**

***Index Terms*—Air-gap eccentricity, fault diagnosis, induction motor drives, position estimation.**

I. Introduction

HIGH air-gap eccentricity values on induction motors (IM) produce unbalanced radial forces that can cause stator to rotor rub. This fact may be traduced in high costs due to motor repair and the stop time of the process or the production line. For such reasons, motor drive manufacturers are deeply interested in including diagnosis functions in the control software to decrease the machine down time and increase the product benefits [1].

There are several proposals designed for detecting faults on IM. However, only few of them are specifically designed for variable speed drives [2]. The strategies based on motor-current-signal analysis (MCSA) for air-gap eccentricity diagnosis are designed for grid-connected motors [3]. Consequently, both speed variations and the components of different frequency currents introduced by the inverter may complicate the application of such strategies.

In [4] and [5], strategies based on the effect of the motor saliencies were proposed for broken rotor bars diagnosis. A similar strategy was proposed in [6] for on-line stator winding fault diagnosis. The information from the motor saliencies is obtained by adding an additional excitation to the fundamental one. These strategies have been previously used for position estimation in close-loop IM drives. In some cases, the additional excitation signals are high-frequency three-phase currents or voltages, added to the machine main excitation. In some others, they are discrete voltage pulses, generated by the inverter while the fundamental excitation is canceled. The air-gap eccentricity is a saliency that modifies the IM parameters. Consequently, the previous strategies could be applied for air-gap eccentricity detection and diagnosis.

In order to evaluate the feasibility of these strategies for air-gap eccentricity diagnosis, an IM model that considers the effects of different saliencies is needed. The saliencies to be modeled are not only those that provide information about the rotor position but also those generated from fault. In [7], an IM model based on multiple-coupled circuits was presented. In addition, a method known as *Winding Function Approach* (WFA), to calculate mutual inductances, was introduced. Regarding the model, all the winding distribution harmonics are taken into account, with no restrictions about stator winding and rotor bar symmetry. A new method to calculate inductances, known as *Modified Winding Function Approach* (MWFA), is proposed in [8]. This method was applied to analyze IM with static, dynamic, or mixed eccentricity in [9] and [10]. An extension of this method was proposed in [11]. It allows obtaining inductances taking radial and axial nonuniformity of both windings and air-gap into account. For this reason, it is possible to include eccentricity and skew effects in the inductance calculation.

The application of the multiple-coupled circuit model to the analysis of a position estimation strategy was presented in [12]. This strategy is based on the effects of winding distribution and rotor bars on the motor zero-sequence voltage, when the motor is excited with a preestablished pulse sequence applied by the inverter [13], [14].

In this paper, the air-gap eccentricity effect on the zero-sequence-voltage signals, when the motor is excited with a

Manuscript received August 29, 2003; revised June 5, 2005. This work was supported in part by Universidad Nacional de Río Cuarto (UNRC), Universidad Nacional de La Plata (UNLP), Universidad Nacional del Sur (UNS), ANPCyT and CONICET. Paper no. TEC-00224-2003.

G. Bossio, C. De Angelo, and G. O. García are with the CONICET, and also with the Grupo de Electrónica Aplicada (GEA), Facultad de Ingeniería, Universidad Nacional de Río Cuarto, X5804BYA, Río Cuarto, Argentina (e-mail: gbossio@ing.unrc.edu.ar; cdeangelo@ieee.org; g.garcia@ieee.org).

J. Solsona is with the CONICET, and also with the Instituto de Investigaciones en Ingeniería Eléctrica "Alfredo Desages," Departamento de Ingeniería Eléctrica y de Computadoras, Universidad Nacional del Sur (UNS), 8000 Bahía Blanca, Argentina (e-mail: jsolsona@uns.edu.ar).

M. I. Valla is with the Laboratorio de Electrónica Industrial, Control e Instrumentación (LEICI), Departamento de Electrotecnia, Facultad de Ingenieria, Universidad Nacional de La Plata (UNLP), 1900 La Plata, Argentina, and also with the CONICET (e-mail: m.i.valla@ieee.org).

Digital Object Identifier 10.1109/TEC.2006.874218

preestablished pulse sequence, is analyzed using the extension of the MWFA, proposed in [11].

The effects on the diagnosis signals of different winding connections are presented. The winding connections considered are series and series–parallel. The series–parallel winding connection is a common practice. It reduces the net unbalanced magnetic pull [15], and allows the construction of only one motor for different voltages, thus changing only the winding connection (e.g., 220 V in series–parallel and 440 V in series).

The paper is organized as follows. A general model for the IM is presented in Section II. In Section III, the inductances for the IM model are obtained. In Section IV, the rotor position estimation strategy is reviewed and static, dynamic, and mixed eccentricity effects are analyzed, using the MWFA. Section V shows experimental results. Finally, discussion and conclusion are given in Section VI.

II. Induction Motor Model

Considering an IM having m stator circuits and n rotor bars, the cage can be viewed as n identical and equally spaced rotor loops [16]. The voltage equations for the IM can be written in vector-matrix form as follows:

$$\mathbf{V}_s = \mathbf{R}_s\mathbf{I}_s + \frac{d\lambda_s}{dt} \tag{1}$$

$$\mathbf{V}_r = \mathbf{R}_r\mathbf{I}_r + \frac{d\lambda_r}{dt} \tag{2}$$

where

$$\mathbf{V}_s = [v_1^s \quad v_2^s \quad \cdots \quad v_m^s]^T, \quad \mathbf{V}_r = [0 \quad 0 \quad \cdots \quad 0]^T \tag{3}$$

$$\mathbf{I}_s = [i_1^s \quad i_2^s \quad \cdots \quad i_m^s]^T, \quad \mathbf{I}_r = [i_1^r \quad i_2^r \quad \cdots \quad i_n^r]^T \tag{4}$$

and the stator and rotor flux linkages are given by

$$\lambda_s = \mathbf{L}_{ss}\mathbf{I}_s + \mathbf{L}_{sr}\mathbf{I}_r \tag{5}$$

$$\lambda_r = \mathbf{L}_{rs}\mathbf{I}_s + \mathbf{L}_{rr}\mathbf{I}_r \tag{6}$$

$\mathbf{L}_{ss}$ is an $m \times m$ matrix with the stator self and mutual inductances, $\mathbf{L}_{rr}$ is an $n \times n$ matrix with the rotor self and mutual inductances, $\mathbf{L}_{sr}$ is an $m \times n$ matrix composed by the mutual inductances between the stator phases and the rotor loops, $\mathbf{L}_{rs}$ is an $n \times m$ matrix composed by the mutual inductances between the rotor loops and the stator phases and $\mathbf{L}_{sr} = \mathbf{L}_{rs}^T$.

III. Inductance Calculations

The mutual inductances used in the proposed multiple-coupled circuit model can be obtained from the equations shown in [11]. According to the present proposal, the mutual inductance between the two stator windings, two rotor loops as well as the mutual inductance between the stator and rotor circuits, A and B, can be obtained from

$$L_{BA}(\theta_r) = \mu_0 r \int_0^{2\pi}\int_0^{L} n_B(\phi, z, \theta_r) N_A(\phi, z, \theta_r) \times g^{-1}(\phi, z, \theta_r)\, dz\, d\phi \tag{7}$$

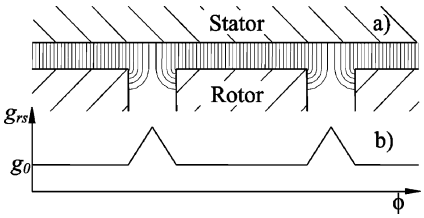

Fig. 1. (a) Flux lines distribution on the air-gap. (b) Air-gap function.

where μ_0 is the air permeability, r is the air-gap average radius, ϕ and z are the angular and axial position of an air-gap arbitrary point, respectively, $g^{-1}(\phi, z, \theta_r)$ is the inverse of the air-gap function, $n(\phi, z, \theta_r)$ is the *winding spatial distribution*, and $N(\phi, z, \theta_r)$ is the *two-dimensional (2-D) modified winding function*. The latter can be obtained as

$$N(\phi, z, \theta_r) = n(\phi, z, \theta_r) - \frac{1}{2\pi L\langle g^{-1}(\phi, z, \theta_r)\rangle} \times \int_0^{2\pi}\int_0^{L} n(\phi, z, \theta_r) g^{-1}(\phi, z, \theta_r)\, dz\, d\phi \tag{8}$$

where $\langle g^{-1}(\phi, z, \theta_r)\rangle$ is an average value of the inverse air-gap function. The distribution of bars and windings, modeled by means of winding spatial distribution functions, were considered for the calculation of inductances in the previous equations. Regarding the bar distribution, skew effects are included as proposed in [11].

A. Rotor Slot Modeling

The air-gap variation, due to rotor slots, was modeled by considering the distribution of the flux lines on the slots [Fig. 1(a)], as proposed in [17]. According to this flux line distribution, the air-gap function considering the rotor slots, g_{rs}, rises linearly from one side to the center of the slot and then drops up to its nominal value, g_0, at the other slot side, as shown in Fig. 1(b) for a rotor and an axial position (θ_{r0}, z_0). Then, the air-gap length can be expressed as

$$g_{rs}(\phi, \theta_r, z) = g_0 + \Delta g_{rs}(\phi, \theta_r, z) \tag{9}$$

where $\Delta g_{rs}(\phi, \theta_r, z)$ is the increment of the flux path in front of a rotor slots.

Stator-slot effects may be included in the same way as rotor-slot effects. However, since slots are uniformly distributed, and the air-gap variation they produce does not depend on rotor position, these slots do not produce any affect on the diagnosis signals. For such reason, the stator-slot effects have not been included in the model.

B. Air-Gap Eccentricity Modeling

In practice, static and dynamic air-gap eccentricities appear in a mixed form [10]. The air-gap function for a mixed eccentricity can be represented by

$$g_e(\phi, \theta_r, z) = g_0[1 - e_s(z)\cos\phi - e_d(z)\cos(\phi - \theta_r)] \tag{10}$$

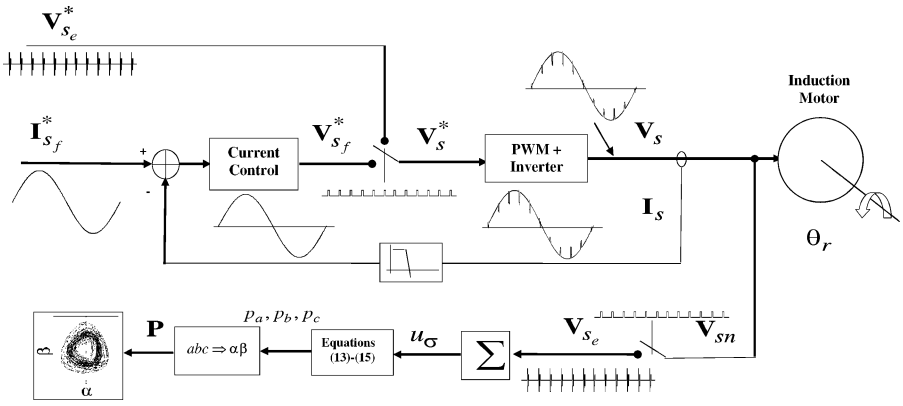

Fig. 2. General scheme of the diagnosis strategy.

where e_s and e_d are the static and dynamic eccentricity amounts, respectively. This equation is used in (7) and (8) for calculating the IM self and mutual inductances with air-gap eccentricity. The combined effects of air-gap eccentricity and rotor slots can also be analyzed. For this purpose, the variation of the air-gap function due to rotor slots, Δg_{rs}, is added to the air-gap function (10), yielding

$$g(\phi, \theta_r, z) = g_e(\phi, \theta_r, z) + \Delta g_{rs}(\phi, \theta_r, z) \tag{11}$$

IV. Analysis of Air-Gap Eccentricity Effects on the Zero-Sequence Voltage when Exciting the Motor with an Additional Excitation

Considering a star-connected IM fed by a three-phase inverter motor saliencies such as air-gap eccentricity affect the zero-sequence voltage. Using an additional excitation to the fundamental one, it is possible to extract information about the saliencies from the zero-sequence voltage. The additional excitation used in this paper for the air-gap eccentricity diagnosis consists in a predefined inverter-switching pattern applied to the motor for a short time while the fundamental excitation is canceled. This excitation was used previously to implement a position estimation strategy [13].

A scheme of the proposed strategy is shown in Fig. 2. In order to inject the additional excitation signal $\mathbf{V}^*_{se}$, the fundamental current control loop $\mathbf{I}^*_{sf}$ is opened for a short-time, while the signal $\mathbf{V}^*_{se}$ takes the control of the pulse width modulation (PWM). The additional excitation signal consists of the six active inverter switching states applied in the following sequence $u_1(+--), u_4(-++), u_3(-+-), u_6(+-+), u_5(--+)$ and $u_2(++-)$ [13].

The zero-sequence voltage is obtained from the sum of the three-phases voltages with respect to the motor neutral point $\mathbf{V}_{sn} = [v_a v_b v_c]$

$$u_\sigma = v_a + v_b + v_c. \tag{12}$$

These voltages are measured synchronized with the injected voltage pulses.

Subtracting the zero-sequence voltages in the opposed switching states.

$$p_a(\theta_r) = u_\sigma^{(1)} - u_\sigma^{(4)} \tag{13}$$

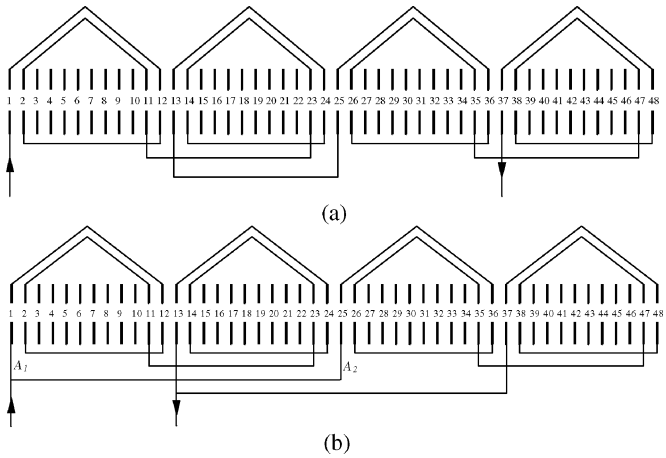

Fig. 3. Coil distribution of phase A. (a) Series connection. (b) Series–parrallel connection.

$$p_b(\theta_r) = u_\sigma^{(3)} - u_\sigma^{(6)} \tag{14}$$

$$p_c(\theta_r) = u_\sigma^{(5)} - u_\sigma^{(2)} \tag{15}$$

where $u_\sigma^{(x)}$ is the zero-sequence voltage corresponding to the u_x switching state. The speed voltage effects are practically eliminated and the voltage signal is a function of the excited phase inductances. For an IM with no faults, these three signals are almost sinusoidal and have n-period-per-revolution, where n is the number of bars.

A spatial vector $\mathbf{P}(\theta_n) = (p_\alpha, p_\beta)$, whose angle provides information about the rotor position, can be obtained by transforming the three-phase signals (13)–(15) into an α and β coordinate system fixed to the stator.

A. Series-Phase Windings

The multiple-coupled circuit model, presented previously, is used to analyze the effect of the motor inductances on the zero-sequence voltage, when the motor was excited with the predefined inverter-switching pattern. For the motor with series phase-winding connection, whose parameters are shown in the Appendix and the coil distribution in Fig. 3(a), $m = 3$ and $n = 40$. Then, the dimensions of the inductance matrices

are $\mathbf{L}_{ss}(3\times 3), \mathbf{L}_{rr}(40\times 40), \mathbf{L}_{sr}(3\times 40)$, and $\mathbf{L}_{rs}(40\times 3)$, respectively.

The estimation signals, p_a, p_b, and p_c are obtained from this model, as proposed by the authors in [12]. If the excitation sequence applied by the inverter corresponds to a small interval of time so that the rotor position and currents remain almost constant, both EMF and the resistance voltage drops can be neglected. From these practical considerations, (1), (2), (5), and (6) can be expressed as

$$\mathbf{V}_s = \mathbf{L}_{ss}\frac{d\mathbf{I}_s}{dt} + \mathbf{L}_{sr}\frac{d\mathbf{I}_r}{dt} \tag{16}$$

$$\mathbf{0} = \mathbf{L}_{rs}\frac{d\mathbf{I}_s}{dt} + \mathbf{L}_{rr}\frac{d\mathbf{I}_r}{dt} \tag{17}$$

solving (17) for the rotor current derivative, and replacing it into (16)

$$\mathbf{V}_s = \left(\mathbf{L}_{ss} - \mathbf{L}_{sr}\,\mathbf{L}_{rr}^{-1}\mathbf{L}_{rs}\right)\frac{d\mathbf{I}_s}{dt}. \tag{18}$$

For switching state $u_1(+--)$, the inverter dc-link voltage, U_d, can be expressed as follows:

$$\begin{aligned} U_d &= v_a - v_b \\ U_d &= v_a - v_c. \end{aligned} \tag{19}$$

The applied voltages resulting from (12) and (19) are

$$v_a = \frac{1}{3}\left(u_\sigma^{(1)} + 2U_d\right) \tag{20}$$

$$v_b = \frac{1}{3}\left(u_\sigma^{(1)} - U_d\right) \tag{21}$$

$$v_c = \frac{1}{3}\left(u_\sigma^{(1)} - U_d\right). \tag{22}$$

Solving for the current derivatives in (18) and replacing the phase voltages by (20)–(22)

$$\frac{d\mathbf{I}_s}{dt} = \frac{1}{3}\left(\mathbf{L}_{ss} - \mathbf{L}_{sr}\mathbf{L}_{rr}^{-1}\mathbf{L}_{rs}\right)^{-1}\left(u_\sigma^{(1)}\mathbf{T}^T + U_d\mathbf{Q}_a^T\right) \tag{23}$$

where

$$\mathbf{T} = [1 \quad 1 \quad 1] \tag{24}$$

$$\mathbf{Q}_a = [2 \quad -1 \quad -1]. \tag{25}$$

Since the sum of currents is equal to zero, premultiplying (23) by $\mathbf{T}$, yields

$$0 = \mathbf{T}\left(\mathbf{L}_{ss} - \mathbf{L}_{sr}\mathbf{L}_{rr}^{-1}\mathbf{L}_{rs}\right)^{-1}\left(u_\sigma^{(1)}\mathbf{T}^T + U_d\mathbf{Q}_a^T\right) \tag{26}$$

Solving for $u_\sigma^{(1)}$, the following expression is obtained:

$$u_\sigma^{(1)} = -U_d\frac{\mathbf{T}\left(\mathbf{L}_{ss} - \mathbf{L}_{sr}\mathbf{L}_{rr}^{-1}\mathbf{L}_{rs}\right)^{-1}\mathbf{Q}_a^T}{\mathbf{T}\left(\mathbf{L}_{ss} - \mathbf{L}_{sr}\mathbf{L}_{rr}^{-1}\mathbf{L}_{rs}\right)^{-1}\mathbf{T}^T} \tag{27}$$

Calculating $u_\sigma^{(4)}$in a similar way, the signal p_a can be determined through (13)

$$p_a = -2U_d\frac{\mathbf{T}\left(\mathbf{L}_{ss} - \mathbf{L}_{sr}\mathbf{L}_{rr}^{-1}\mathbf{L}_{rs}\right)^{-1}\mathbf{Q}_a^T}{\mathbf{T}(\mathbf{L}_{ss} - \mathbf{L}_{sr}\mathbf{L}_{rr}^{-1}\mathbf{L}_{rs})^{-1}\mathbf{T}^T} \tag{28}$$

Equations needed to obtain p_b and p_c are similar to (28), changing only the column vector in the numerator, $\mathbf{Q}$:

$$\mathbf{Q}_b = [-1 \quad 2 \quad -1] \tag{29}$$

$$\mathbf{Q}_c = [-1 \quad -1 \quad 2] \tag{30}$$

The p_a, p_b, and p_c signals were calculated for a three-phase motor whose parameters are shown in the Appendix. These signals showed a 40-cycle-per-revolution component due to the inductance variations. Such variations are produced by the discrete distribution of the 40 rotor bars and by the air-gap variation due to the rotor slots [12]. These signals also presented a 120° displacement due to the spatial distribution of each phase.

Transforming the three-phase signals into the α and β coordinate system fixed to the stator, the signals p_β versus p_α, can be obtained from the proposed model, as shown in Fig. 4(a). This figure also shows the p_α signal spectrum, where the 40-cycle-per-revolution component can be clearly observed.

Fig. 4(b) shows the effect produced by a 60% static eccentricity $(e_s = 0.6)$, with a rotor displacement in the phase-a direction. Due to this eccentricity, a dc component appears on the estimation signals, which points out the rotor-displacement direction in the p_β versus p_α plane. In addition, the 40-cycle-per-revolution fundamental signal is slightly increased.

Fig. 4(c) shows p_β versus p_α signals with 60% of dynamic eccentricity $(e_d = 0.6)$. As it can be seen in the p_α signal spectrum, dynamic eccentricity produces a four-cycle-per revolution component due to the air-gap periodic variation in each of the four poles. In addition, a slight increase in the fundamental component can be seen in the signal spectrum.

In practice, dynamic eccentricity is generally produced by bearing wear, misalignment, or bent rotor shaft. In these particular cases, eccentricity is nonuniform along the motor axial length. As a consequence, high eccentricity levels will appear on one of the rotor end whereas low levels of eccentricity will appear on the other, then producing components of lower amplitude on the diagnosis signals than those produced by a uniform eccentricity. For such reason, and in order to compare the results obtained by using the multiple-coupled circuit model and those obtained experimentally, a mixed air-gap eccentricity was modeled as

$$e_d(z) = e_{d0} + k_e z \tag{31}$$

$$e_s(z) = e_{s0} \tag{32}$$

where

$$e_{d0} = 0.29, \quad k_e = 3.85, \quad e_{s0} = 0.1. \tag{33}$$

These coefficients correspond to both an added nonuniform dynamic eccentricity of the motor (29% in $z = 0$ and 71% in $z = L$) and an inherent level of static eccentricity (10%). The dynamic eccentricity corresponds to the produced by the bushing a_2 described in the Section V.

Fig. 4(d) shows p_β versus p_α signals and the p_α signal spectrum for mixed eccentricity. Unlike dynamic or static eccentricity, mixed eccentricity produces several low-frequency harmonics. A four-cycle-per-revolution component, as for dynamic eccentricity, can be appreciated in the low-frequency signal

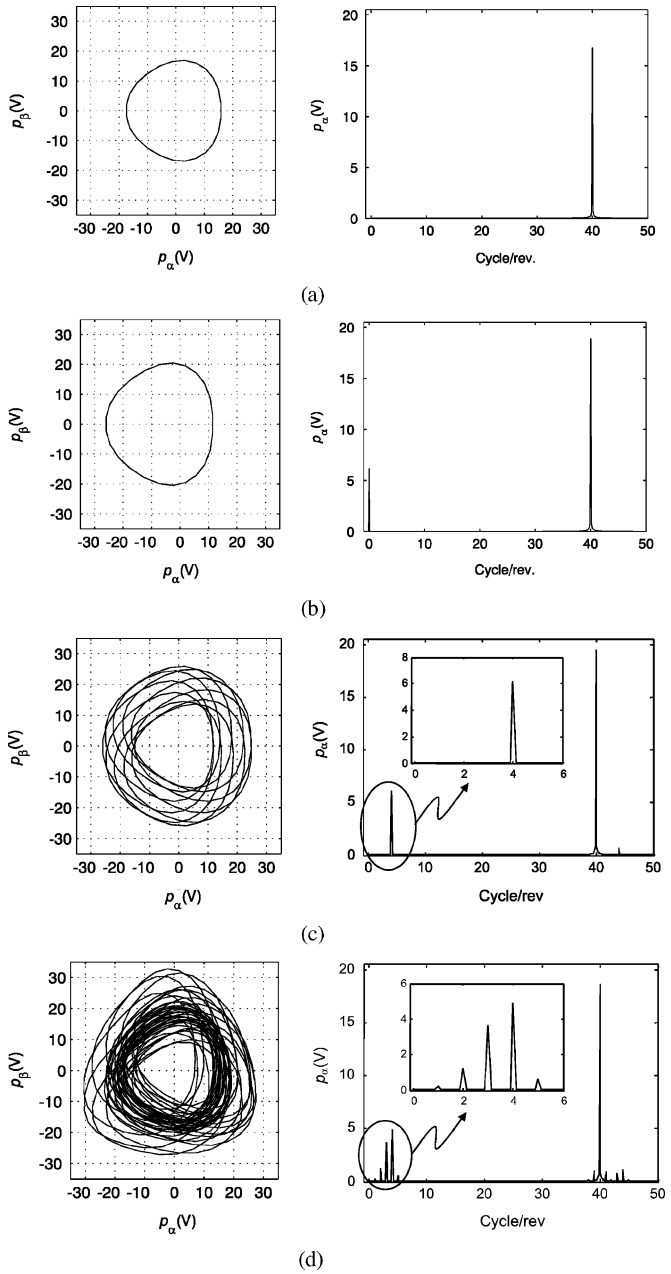

Fig. 4. Simulation result. Signals p_β versus p_α and p_α signal spectrum, series phase windings. (a) With no eccentricity. (b) With 60% static eccentricity. (c) With 60% dynamic eccentricity. (d) With mixed eccentricity.

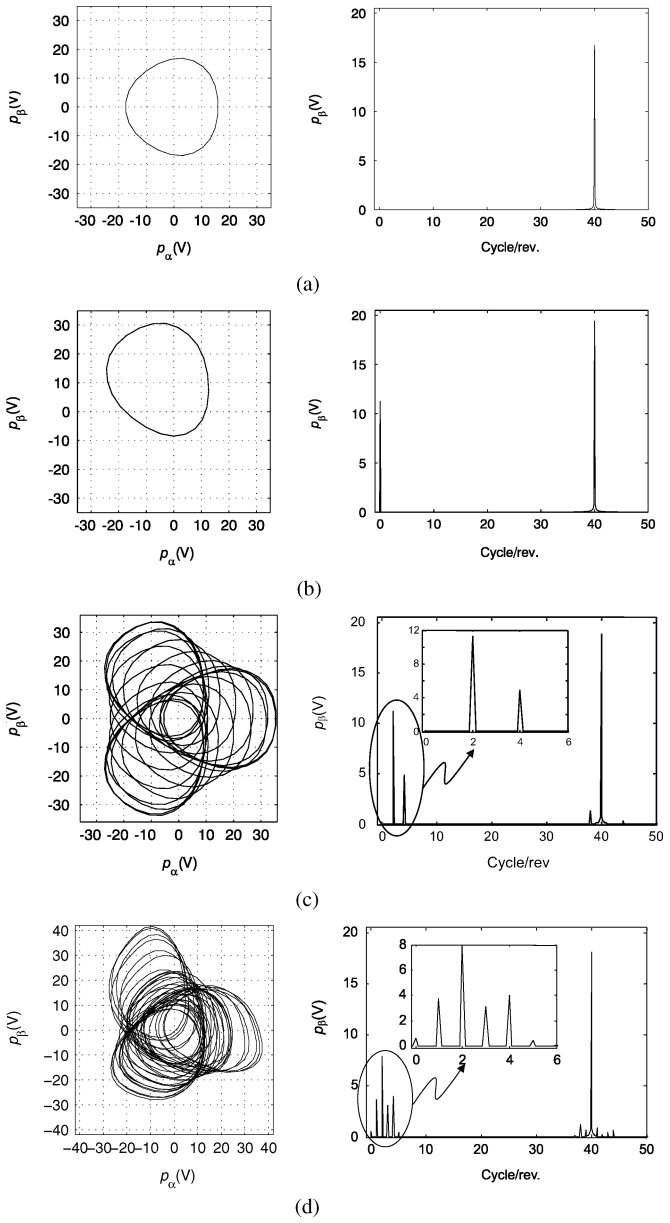

Fig. 5. Simulation result. p_β versus p_α signals, and p_β signal spectrum, series–parallel phase windings. (a) With no eccentricity. (b) With 60% static eccentricity. (c) With 60% dynamic eccentricity. (d) With mixed eccentricity.

spectrum. The dc component is very low due to the low level of static eccentricity considered in this case. In addition, 1, 2, and 3-cycle-per-revolution components appear in the signal spectrum due to the combination of static and dynamic eccentricity effects.

B. Series–Parallel Phase Windings

The series–parallel phase winding motor has the same parameters than the series phase winding motor and differs only in the phase winding connection. The in-series–parallel winding connection of phase A is shown in Fig. 3(b). For this motor, $m = 6$ and $n = 40$. Then, the dimensions of the inductance matrices are: $\mathbf{L}_{ss}\ (6 \times 6), \mathbf{L}_{rr}(40 \times 40), \mathbf{L}_{sr}(6 \times 40)$, and $\mathbf{L}_{rs}(40 \times 6)$, respectively.

For this windings connection, the estimation signals, using the multiple-coupled circuit model, can be obtained in a way similar to what the authors proposed in [12]. The p_a signal is given by (28), where

$$\mathbf{T} = [1 \quad 1 \quad 1 \quad 1 \quad 1 \quad 1] \tag{34}$$

$$\mathbf{Q}_a = [2 \quad 2 \quad -1 \quad -1 \quad -1 \quad -1] \tag{35}$$

Fig. 5(a) shows p_β versus p_α signals and the p_β signal spectrum for the motor with no eccentricity. As in the case of series phase windings, a 40-cycle-per-revolution component appears.

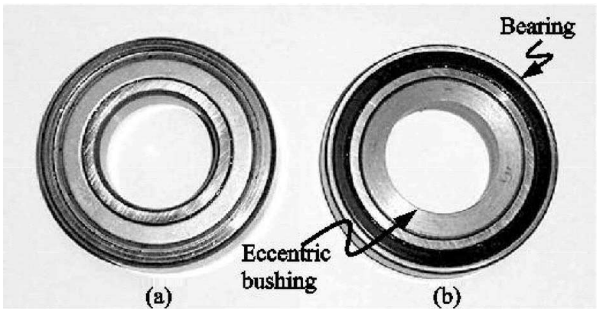

Fig. 6. (a) Original bearing. (b) Bearing and eccentric bushing.

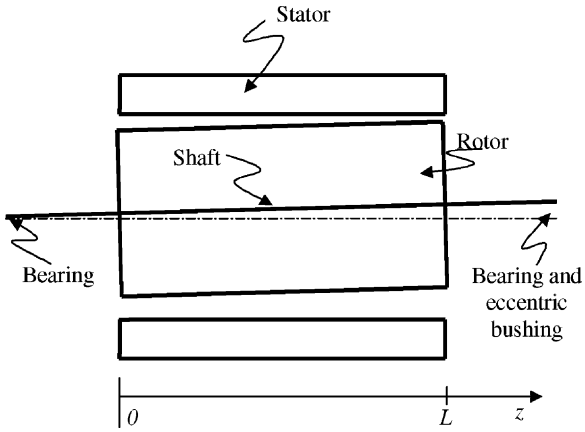

Fig. 7. Nonuniform air-gap eccentricity.

The series–parallel connection does not affect the amplitude of this signal.

Fig. 5(b) shows the effects of a 60% static eccentricity ($e_s = 0.6$), with rotor displacement in the phase-a direction. Due to this eccentricity, a dc component appears in the estimation signals, but in this case, it does not coincide with the rotor displacement direction as seen in the p_β versus p_α plane. For the same eccentricity, the value of the dc component doubles that produced by in-series-winding connection. The p_β signal spectrum is shown instead of the p_α one, since the dc component is more significant in the β-axis direction.

Fig. 5(c) shows the effect of a 60% dynamic eccentricity ($e_d = 0.6$). The dynamic eccentricity effect on the diagnosis signals differs from that of in-series-winding connection. In this case, two components appear in low frequencies of the signal spectrum. A four-cycle-per-revolution component, as for in-series-winding connections, appears in the spectrum due to air-gap variation in each of the four poles. In addition, a significant two-cycle-per-revolution component is produced by an air-gap periodic variation in each of the two independent phase circuits [Fig. 3(b)]. Apart from that, inductance variation produced by the air-gap eccentricity in each pole is the same in-series and in-series–parallel winding connections. However, for in-series connections, the phase inductance is the sum of each pole inductance and it results in an inductance variation of four-cycle per-revolution. For in-series–parallel connections, the total phase inductance presents a four-cycle per-revolution variation due to each pole and a two-cycle per-revolution variation produced by the two-phase circuits.

The mixed air-gap eccentricity was modeled as in the previous case, considering the same values of dynamic eccentricity and a 10% of static eccentricity. Fig. 5(d) shows p_β versus p_α signals and the p_β signal spectrum for the mixed eccentricity modeled by (31)–(33). An important two-cycles-per-revolution component, as for dynamic eccentricity, can be appreciated in the signal spectrum. A dc component and 1, 3, and 4-cycle-per-revolution components appear in the signal spectrum due to mixed eccentricity.

Comparing these results with those obtained from the motor with series phase windings, it can be observed that although the harmonics produced by eccentricity are the same, the amplitude relations are very different. As it was stated previously, the difference in amplitudes is due to the fact that different stator winding connections have different inductance variations in each phase.

TABLE I
AIR-GAP ECCENTRICITY LEVELS FOR DIFFERENT ECCENTRIC BUSHINGS

Bushing	Eccentricity level	
	z=0	*z=L*
a_1	*19%*	*47.5%*
a_2	*29%*	*71%*
a_3	*33%*	*82%*

V. EXPERIMENTAL RESULTS

The estimation strategy was programmed on a PC, in order to validate the proposed analysis. The references to the excitation signals corresponding to a voltage injection of the switching pattern through the inverter are first generated, and then the software calculates the zero-sequence voltage from the measurements of phase voltages.

In order to produce air-gap dynamic eccentricity, one bearing [Fig. 6(a)] was replaced by another of bigger interior diameter and of equal external diameter plus an eccentric bushing [Fig. 6(b)]. Such a bushing, made of steel, adapts the shaft diameter to the internal bearing diameter. Since only one bearing was modified, the air-gap eccentricity is nonuniform along the motor axial length as shown in Fig. 7. Three bushings with different eccentricity levels were made to evaluate the diagnosis strategy. The air-gap eccentricity levels for these bushing are shown in Table I.

The experimental results shown in this section were obtained with the motor rotating at 30 r/min, without fundamental excitation and load. If the IM is operated at full fundamental excitation (ω_e) and load, an additional component at frequency $2\omega_e$ may appear in the diagnosis signals due to saturation [14]. Depending on the load level, the saturation component may interfere with the component produced by the air-gap dynamic eccentricity. Therefore, in order to implement the strategy for on-line diagnosis, this component due to the fundamental excitation should be decoupled.

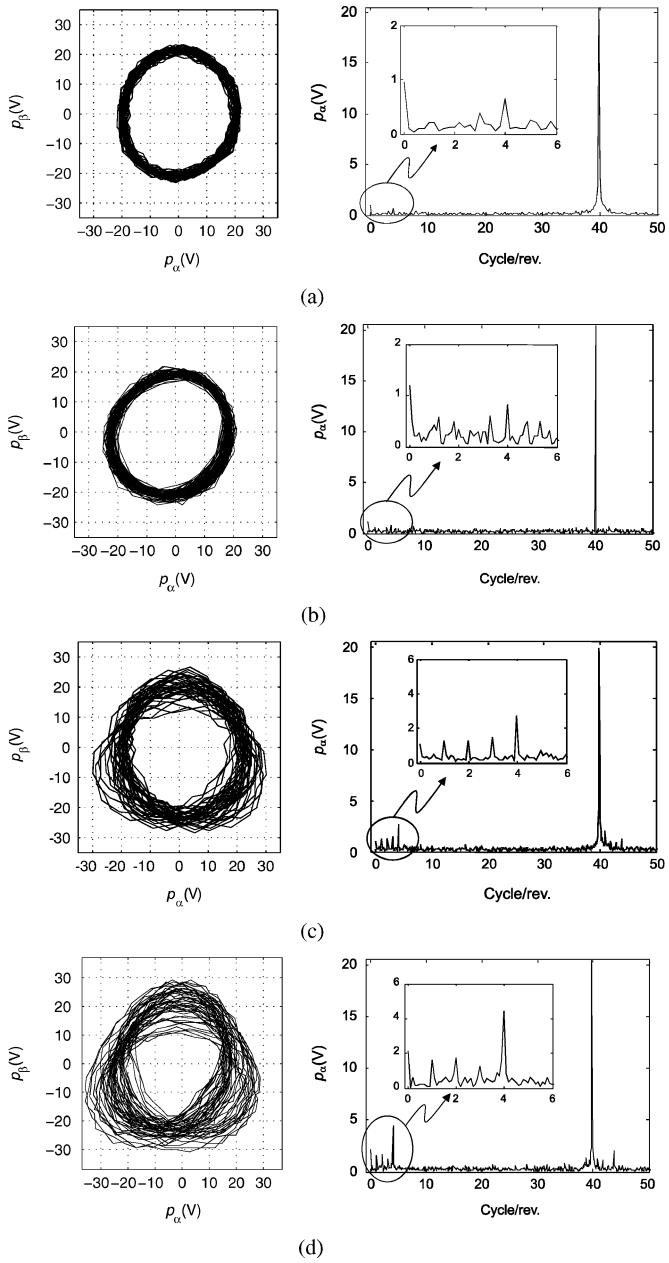

Fig. 8. Experimental result. Signals p_β versus p_α and p_α signal spectrum, series phase winding: (a) Without eccentricity. (b) With mixed eccentricity for the bushing a_1, (c) a_2, and (d) a_3.

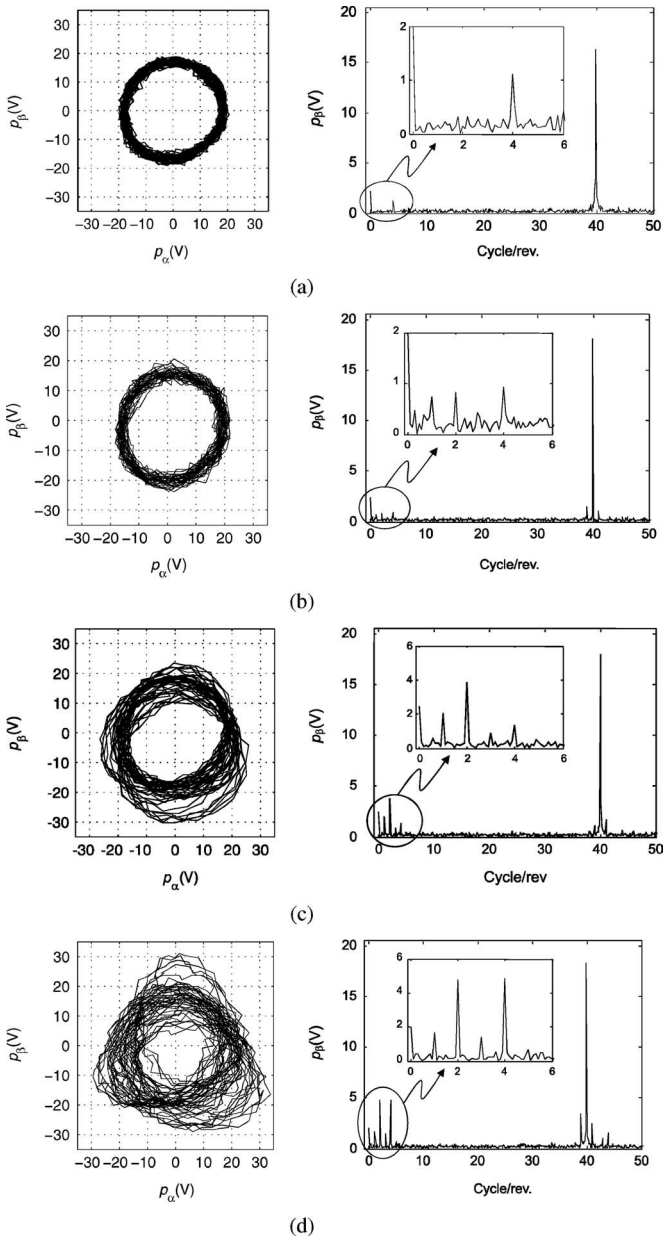

Fig. 9. Experimental result. Signals p_β versus p_α and p_β signal spectrum, series–parallel phase winding: (a) Without eccentricity. (b) With mixed eccentricity for the bushing a_1, (c) a_2, and (d) a_3.

The signals obtained with the series windings motor without eccentricity are first presented. Fig. 8(a) shows the p_β versus p_α signals and the p_α signal spectrum. In addition to the 40-cycle-per-revolution component, produced by the rotor bars, a small four-cycle-per-revolution component can be seen in the signal spectrum. This component could be produced by a rotor inherent asymmetry due to the manufacturing and assembly method.

Fig. 8(b) shows p_β versus p_α signals and the p_α signal spectrum with mixed eccentricity produced by bushing a_1. This low level of eccentricity produces only a very small change in the path of vector $\mathbf{P}$ in the $\alpha - \beta$ plane and in the four-cycle-per-revolution component shown in the p_α signal spectrum.

Fig. 8(c) shows p_β versus p_α with mixed eccentricity produced by the bushing a_2. They are similar to those obtained using the proposed model. Comparing the p_α signal spectrums, shown in Fig. 8(c) and Fig. 4(d), almost the same harmonics appear in the model-based analysis and in the experiments. Fig. 8(d) shows the results obtained with the bushing a_3. From these results, it can be observed that for a small increase of the eccentricity level (in comparison with that produced by bushing a_2), an important modification appear in both, the vector $\mathbf{P}$ path and the four-cycle-per-revolution component amplitude.

In the low-frequency signal spectrum, the harmonic components are the same to that predicted by the model-based analysis. However, their amplitudes are a little smaller. These

low-frequency harmonics can be used for air-gap eccentricity diagnosis using the proposed method.

Fig. 9(a) shows the p_β versus p_α signals and the p_β signal spectrum for the series–parallel winding motor with no eccentricity. The signal amplitude, due to the rotor bars, is a little smaller than the one obtained with series-winding motor. Fig. 9(b)–(d) show the signals p_β versus p_α and the p_β signal spectrum for the series–parallel winding motor with air-gap eccentricity produced by the bushings a_1, a_2, and a_3 respectively. As for the series-winding motor, bushing a_1 produces a small change in the path of vector $\mathbf{P}$ in $\alpha - \beta$ plane, even when the relation between the amplitudes of the low-frequency components, shown in the spectrum, are different.

For the results shown in Fig. 9(c) and (d), the harmonics are the same as those predicted by the model-based analysis.

Although almost the same harmonics appear in the signal spectrum, the signals in the plane, obtained from the model [Fig. 5(d)], look different from the experimental results. This is due to the fact that the amplitude of each component, obtained experimentally, is smaller than that obtained from the model-based analysis. In addition, the value, direction, and distribution of the inherent level of static eccentricity are unknown and they probably differ from the values considered in the model.

From the experimental results obtained in this section, it can be observed that the detection of eccentricity in the air-gap using the proposed strategy is possible. The diagnosis signals for motor without eccentricity show a component whose number of cycles is the same as the number of rotor bars. Although this component does not vary significantly for an increase in the air-gap eccentricity, new low-frequency components appear. The relation between amplitudes of these harmonics differs for in-series and in-series–parallel windings.

The relation between amplitudes of these harmonics differs for the two types of windings. However, in both cases, a component with a number of cycles per revolution equal to the number of motor poles (four in this case) appears as a consequence of eccentricity. Moreover, in the case of in-series–parallel windings, it appears another component in the spectrum which corresponds with the number of in-parallel circuits the phase has (two cycles per revolution in this case).

VI. Discussion And Conclusion

In this work, the air-gap eccentricity effects on the zero-sequence voltage signals, when the induction motor is excited with a preestablished pulse sequence applied by the inverter, were analyzed. The results showed that such faults produce significant changes on the diagnosis signals. Consequently, the fault diagnosis and detection from these signals is quite feasible. The stator windings configurations affect the diagnosis signal, changing the amplitude and frequency of the harmonic components. Experimental results showed the feasibility of this proposal.

In order to implement this strategy for on-line diagnosis, the effects due to the fundamental excitation and load should be analyzed. However, the diagnosis strategy can be easily implemented as a self-commissioning scheme in order to detect air-gap eccentricity.

Appendix

Motor Data

- Nominal power: 5.5 kW; pair of poles: 2.
- Stator winding: 34 turns per coil, two coil per group, four groups per phase, step 1:10:12.
- Number of stator slots: 48; number of rotor bars: 40.
- Air-gap: 0.45 mm; stator length (L): 0.11 m.
- Air-gap average radius: 0.075 m.
- Skewing: One stator slot period.
- Rotor slot opening: 2.5 mm.

References

[1] S. Nandi and H. Toliyat, "Condition monitoring and fault diagnosis of electrical machines—A review," in *Proc. IEEE-IAS Annu. Meeting*, 1999, vol. 1, pp. 197–204.

[2] R. Wieser, C. Kral, F. Pirker, and M. Schagginger, "On-line rotor cage monitoring of inverter-fed induction machines by means of an improved method," *IEEE Trans. Power Electron.*, vol. 14, no. 5, pp. 858–865, Sep. 1999.

[3] P. Vas, *Parameter Estimation, Condition Monitoring, and Diagnosis of Electrical Machines*. Oxford: Clarendon Press, 1993.

[4] A. Bellini, G. Franceschini, N. Petrolini, C. Tassoni, and F. Filippetti, "On-line diagnosis of induction drives rotor by signal injection techniques: Faults location and severity classification," presented at the IEEE SDEMPED, Grado (Go), Italy, 2001.

[5] ——, "Induction machine rotor position detection for diagnostic or control AIMS: Possibilities and problems," presented at the 9th Eur. Conf. Power Electronics and Applications, Graz, Aug. 2001.

[6] F. Briz, M. W. Degner, A. Zamarrón , and J. M. Guerrero, "On line stator winding fault diagnosis in inverter-fed ac machines using high-frequency signal injection," *IEEE Trans. Ind. Appl.*, vol. 39, no. 4, pp. 1109–1117, Jul.–Aug. 2003.

[7] H. A. Toliyat, T. A. Lipo, and J. C. White, "Analysis of a concentrated winding induction machine for adjustable speed drive applications—Part I (Motor Analysis)," *IEEE Trans. Energy Convers.*, vol. 6, no. 4, pp. 679–692, Dec. 1991.

[8] N. A. Al Nuaim and H. A. Toliyat, "A novel method for modeling dynamic air-gap eccentricity in synchronous machines based on modified winding function theory," *IEEE Trans. Energy Convers.*, vol. 13, no. 2, pp. 156–162, Jun. 1998.

[9] S. Nandi and H. Toliyat, "Detection of rotor slot and other eccentricity related harmonics in a three phase induction motor with different rotor," *IEEE Trans. Energy Convers.*, vol. 16, no. 3, pp. 253–260, 2001.

[10] S. Nandi, R. Bharadwaj, and H. Toliyat, "Perfomance analysis of a three phase induction motor under mixed eccentricity condition," *IEEE Trans. Energy Convers.*, vol. 17, no. 3, pp. 392—399, Sep. 2002.

[11] G. Bossio, C. De Angelo, J. Solsona, G. García, and M. I. Valla, "A 2D-model of the induction motor: An extension of the modified winding function approach," *IEEE Trans. Energy Convers.*, vol. 19, no. 1, pp. 144–150, Mar. 2004.

[12] G. Bossio, C. De Angelo, J. Solsona, G. García, and M. Valla, "Analysis of a position estimation strategy using a multiple-coupled circuits model of the induction motor," in *Proc. IEEE 28th Annu. Conf. IECON*, Sevilla, Spain, Nov. 5–8, 2002, pp. 822–827.

[13] J. Jiang and J. Holtz, "Accurate estimation of rotor position and speed of induction motors near standstill," in *Proc. IEEE Int. Conf. PEDS*, Singapore, 1997, pp. 1–5.

[14] J. Holtz, "Sensorless position control of induction motors-An emerging technology," *IEEE Trans. Ind. Electron.*, vol. 45, no. 6, pp. 840–851, Dec. 1998.

[15] M. J. DeBortoli, S. J. Salon, D. W. Burow, and C. J. Slavik, "Effects of rotor eccentricity and parallel windings on induction machine behavior: A study using finite element analysis," *IEEE Trans. Magn.*, vol. 29, no. 2, pp. 1676–1682, Mar. 1993.

[16] X. Luo, Y. Liao, H. Toliyat, A. El-Antably, and T. A. Lipo, "Multiple-coupled circuit modeling of induction machines," *IEEE Trans. Ind. Appl.*, vol. 31, no. 2, pp. 311–318, Mar.–Apr. 1995.

[17] T. Lipo, *Introduction to ac Machine Design,* Madison, WI: Wisconsin Power Electronics Research Center, pp. 79–80, 1996.

Guillermo Bossio (S'03) received the electrical engineer degree from the National University of Río Cuarto, Río Cuarto, Argentina, in 1999, and the Dr. Eng. degree from the National University of La Plata, La Plata, Argentina, in 2004.

Currently, he is with CONICET, and also with the Grupo de Electrónica Aplicada, Facultad de Ingeniería, Universidad Nacional de Río Cuarto, Río Cuarto, Argentina. His research interests include electric machines and drives, fault diagnosis in electric machines, and sensorless motor control.

Cristian De Angelo (S'96–M'05) received the electrical engineer degree from the National University of Río Cuarto, Río Cuarto, Argentina, in 1999, and the Dr. Eng. degree from the National University of La Plata, La Plata, Argentina, in 2004.

Currently, he is with the CONICET, and also with the Grupo de Electrónica Aplicada, Facultad de Ingeniería, Universidad Nacional de Río Cuarto, Río Cuarto. His research interests include power electronics, sensorless motor control, electric vehicles, and renewable energy generation.

Jorge Solsona (S'94–M'96–SM'04) received the electronics engineer and Dr. Eng. degrees from the Universidad Nacional de La Plata, La Plata, Argentina, in 1986 and 1995, respectively.

Currently, he is with the Instituto de Investigaciones en Ingeniería Eléctrica "Alfredo Desages," Departamento de Ingeniería Eléctrica y de Computadoras, Universidad Nacional del Sur, Bahía Blanca, Argentina, where he is involved in teaching and research on control theory and its applications to electromechanical systems.

Guillermo O. García (M'86–SM'01) received the electrical and electronics engineering degree from the National University of Cordoba, Cordoba, Argentina, in 1981, the M.Sc. and Dr. Eng. degree in electrical engineering from COPPE, Federal University of Rio de Janeiro, Rio de Janeiro, Brazil, in 1990 and 1994, respectively.

Currently, he is the Director of the Applied Electronics Group and Professor at the Electrical and Electronics Department, National University of Río Cuarto, Río Cuarto, and also with CONICET. His research interests include power electronics, motion control, electric vehicles, and renewable energy conversion.

María I. Valla (S'79–M'80–SM'97) received the electronics engineering, and the Dr. Eng. degrees from the National University of La Plata (UNLP), La Plata, Argentina, in 1980 and 1994, respectively.

Currently, she is working as a Professor at the Electrical Engineering Department, Engineering Faculty, UNLP, where she is engaged in teaching and research on power converters and ac motor drives, and also with CONICET.